

## Article

# Thyroxine Quantification by Using Plasmonic Nanoparticles as SERS Substrates

Paulina De Leon Portilla <sup>1,2</sup> , Ana L. González <sup>2</sup> and Enrique Sanchez-Mora <sup>1,\*</sup>

<sup>1</sup> Instituto de Física-Ecocampus Valsequillo, Benemérita Universidad Autónoma de Puebla, Independencia O 2 Sur No. 50, San Pedro Zacachimalpa, 72960 Puebla, Mexico; pdeleon@ifuap.buap.mx

<sup>2</sup> Instituto de Física, Benemérita Universidad Autónoma de Puebla, Av. San Claudio y 18 Sur, Ciudad Universitaria, 72570 Puebla, Mexico; ana.gonzalezron@correo.buap.mx

\* Correspondence: enrique.sanchez@correo.buap.mx

**Abstract:** Functionalized Au and Ag nanoparticles (NPs) with ascorbic and tannic acid, respectively, were used as SERS substrates (SS). Several SS were fabricated with different loads of metal NPs deposited on silicon wafers. We focused on the thyroxine (T4) band at  $1044\text{ cm}^{-1}$  and tracked its intensity and position at concentrations from 10 pM to 1 mM. For all SS, the band intensity decreased as the T4 concentration decreased. Additionally, the band shifted to larger wavenumbers as the NP loads increased. In the case of Au, the SS with the highest load of NPs, the minimum concentration detected was 1  $\mu\text{M}$ . The same load of the Ag NP SS showed a better performance detecting a concentration of 10 pM, an outcome from a SERS-EF of  $10^9$ . The NP spatial distribution includes mainly isolated NPs, quasi-spherical clusters, and semi-linear arrays of NPs in random orientations. From the numerical simulations, we conclude that the hot spots at the interparticle gaps in a linear array of three NPs are the most intense. The Ag NP SS demonstrated good sensitivity, to allow the detection of pM concentrations. Therefore, its complementation to any immunoassay technique provides an interesting alternative for point-of-care implementations, such as test strips.

**Keywords:** thyroxine quantification; functionalized nanoparticles; load of nanoparticles; wavenumber shift in SERS; hot spots



**Citation:** De Leon Portilla, P.; González, A.L.; Sanchez-Mora, E. Thyroxine Quantification by Using Plasmonic Nanoparticles as SERS Substrates. *Chemosensors* **2023**, *11*, 516. <https://doi.org/10.3390/chemosensors11100516>

Academic Editors: Cristina M. Muntean and Chung-Wei Kung

Received: 3 June 2023

Revised: 1 August 2023

Accepted: 30 August 2023

Published: 30 September 2023



**Copyright:** © 2023 by the authors. Licensee MDPI, Basel, Switzerland. This article is an open access article distributed under the terms and conditions of the Creative Commons Attribution (CC BY) license (<https://creativecommons.org/licenses/by/4.0/>).

## 1. Introduction

Thyroxine (T4) is a hormone, which is secreted by the thyroid gland and is made up of phenyls, iodine, carboxyl, hydroxyl, ether, and amino groups. T4 is crucial for the right development of reproductive organs, neurons, etc. [1,2], in addition to, for the proper functioning of the human body. A deficiency ( $T4 < 64\text{ nM}$ ) promotes growth issues in humans, whereas in excess ( $T4 > 141\text{ nM}$ ), it contributes to the development of various diseases, such as thyroiditis, and cancer nodules, among others [2,3]. Therefore, it is vital to detect concentration levels of T4 out of the normal range in the bloodstream. Additionally, focusing attention on the T4 hormone (free or bound), it is important to track triiodothyronine (T3)—both bound and free forms—the thyroid stimulating hormone (TSH, also named thyrotropin), and the thyroid releasing hormone (TRH), to make a proper diagnosis of thyroid gland function. As reference values, we can indicate normal, hypothyroid, and hyperthyroid hormone conditions at 1.2 ng/mL, 0.2 ng/mL, and 2.2 ng/mL, respectively, for the T3 concentration, and 70 ng/mL, 30 ng/mL, and 140 ng/mL for the T4 concentration, respectively [4]. Normal ranges for thyroid tests may vary slightly among different laboratories. In [5], the normal values are indicated as 0.5 to 5.0 mIU/L for TSH, 0.7 to 1.9 ng/dL for FT4 (free T4), 5.0 to 12.0  $\mu\text{g/dL}$  for total T4, and 80.0 to 220 ng/dL for total T3.

The T3, T4, and TSH concentrations are routinely measured by a blood test. Some clinical tests are based on the use of radioimmunoassay and immunoradiometric analyses.

Using these methods, it has been possible to detect FT3, FT4, and TSH at normal and hypothyroidism levels [4,6–9]. However, some drawbacks of these tests are that patients may receive intravenous iodine as a contrast medium before the serum thyroxine test, long assay and sample preparation times, expensive instruments, and the employment of radioactive tracers. At the research level, innumerable efforts have been made to improve the precision and accuracy of measurements, especially at low concentrations, by looking for simple, reliable, and label-free methods. Literature can be found that reports on thyroid hormones (a small molecule type) in human or animal serum, urine, or tissues, either in its pure or synthetic form, by using sensors or methods that are the outcome of combining more than two techniques and at least one kind of antibody, all of them with the aim of contributing to the understanding of hypo- and hyperthyroidism. In that sense, a list of techniques includes chromatography coupled with mass spectroscopy [10–15], immunoassays with magnetic or plasmonic nanoparticles [16–18], electrochemical or chemiluminescence techniques complemented with immunoassays and/or nanoparticles [19–24], among others. Some of those techniques require pretreatment, purification, or labeling of the sample, while others use high-pressure conditions, which generate an increase in the analysis costs [10,12,13,16].

Particularly, T4 (free or bound) quantification has reached limits of detection of hundreds of pM [13], tens of pM [22,25], and even a few pM [20]. The common factor in those studies, excluding [13], is the use of nanoparticles, either magnetic or plasmonic. Gold and silver are noble plasmonic metals par excellence; their main feature is the large electric field enhancement on and close to their surface when they are in resonance with the incident light, which gives origin to the electromagnetic mechanism of the surface-enhanced Raman scattering (SERS) phenomenon [26]. SERS occurs when the analyte is in very close proximity to the plasmonic surface, and under in-resonance conditions the Raman signal can be enhanced several orders of magnitude. The most important feature is that the Raman spectrum is specific to each molecule, which is a potential advantage of multiplexed labeling [27].

SERS promoted by Au or Ag NPs and coupled to immunoassays or other analysis techniques has been addressed for sensing macromolecules, such as proteins, viruses, DNA, heavy metals, and tumors [28–30]. By using Au NPs of about 37 nm in diameter, estradiol (limit of detection, LOD, of 2.4 pM) and TSH (LOD of 33  $\mu$ M) hormones have been studied; see [31,32] for details, respectively. S. M. Kim and colleagues reported the detection of T4 with Au–tellurium earthworm-like structures, yet a LOD value was not indicated [33].

Even though SERS is a relatively simple, reliable, and inexpensive technique, the enhancement of the Raman signal (SERS-EF) depends on several key factors, such as the power and wavelength laser, exposure time, the chemical structure and composition of the molecule, and the metal surface roughness [26]. The shape, size, and material of the NPs play a pivotal role in fabricating a vast diversity of SERS substrates. For example, with wire-like clusters of small Ag NPs (size of 17 nm) and a laser of 488 nm, a SERS-EF of  $10^8$ – $10^{10}$  was enough to detect methylene blue molecules [34]. That range of SERS-EF values is sufficient to trace a single molecule. The great performance of that specific Ag structure lies in a large number of hot spots (high-intensity electric field zones), which originate at each interparticle gap (1.7 nm) along the wire-like clusters. With spherical Au NPs of various sizes, from 17 nm to 80 nm, 4-aminothiophenol was detected with SERS-EFs in the order of  $10$ – $10^5$ . From an optimization study of SERS measurements, the optimal Au NP size to obtain the largest SERS-EF was 50 nm; under off-resonance conditions (the laser wavelength was 647 nm) [35].

There are several options for synthesizing metallic NPs that vary in size and shape; some of which are nanolithography techniques [36,37], Turkevich [38], and seed-mediated growth methods [39]. The last is a good option for obtaining spherical Au and Ag NPs; the size can be controlled by the number of growth stages [39,40].

In this work, we report on the detection and quantification of T4 using Au and Ag NPs as SERS platforms. Functionalized spherical NPs of about 50 nm were synthesized by the seed-mediated growth method. Intensity changes and frequency shifts are observed in

the SERS response for SERS substrates (SS) fabricated with different numbers of metal NPs. For an excitation wavelength of 632 nm, Ag NP SS showed a larger sensitivity because the lowest T4 concentration detected with it was 10 pM, while for the Au NP SS, it was 1  $\mu$ M.

Therefore, under specific conditions and without labeling target substances, T4 was successfully detected at levels linked to hypothyroidism conditions, meaning this simple SERS platform is a potential candidate for sensing other small analytes. It is also a prospect to complement immunoassay analysis for sensor devices.

## 2. Materials and Methods

Chloroauric acid (Sigma-Aldrich, St. Louis, MO, USA, 99.9%), L-ascorbic acid (Sigma-Aldrich, 98%), and polyvinylpyrrolidone (PVP, Sigma-Aldrich, average molar weight 10,000) were used to synthesize Au NPs. Ag NPs were obtained using silver nitrate (Riedel-de-Haën, Seelze, HAJ, DE, 98%), tannic acid (Sigma-Aldrich, 99%), and sodium citrate dihydrate (J. T. Baker, Center Valley, PA, USA, 99.98%). To support the NPs, p-type silicon wafers (SW) with a resistivity of 0.01–0.02  $\Omega$  cm were employed. Thyroxine precursor was provided by Sigma-Aldrich (99%).

### 2.1. Au NPs Synthesis

Au NPs were synthesized using the seed-mediated growth method. First, 35 mg of PVP and 60 mg of L-ascorbic acid were mixed in 6 mL of deionized water. Then, 3 mL of chloroauric acid (1 mM) was added to the solution and allowed to react for 3 h to obtain Au seeds. Subsequently, the seeds were subjected to two stages of growth, each one by adding 3 mL of chloroauric acid and giving it 3 h to react. The whole process occurred at a constant temperature of 90  $^{\circ}$ C. Finally, the Au NPs were centrifuged (Hermle LaborTechnik Z 36 HK) at 18,000 rpm for 15 min and redispersed in 20 mL of deionized water (18.2 M $\Omega$  cm).

### 2.2. Ag NPs Synthesis

We followed a previously reported Ag NP synthesis method [41]. Briefly, the procedure is described as follows: Firstly, 50 mL of tannic acid (0.1 mM), 50 mL of sodium citrate (45 mM), and 1 mL of silver nitrate (25 mM) were mixed for 15 min at 90  $^{\circ}$ C. Then, the seed solution was centrifuged to further redisperse it in deionized water. Four growths were made, for each growth 20 mL of the seed solution (0.21 M), 16 mL of deionized water, 500  $\mu$ L of sodium citrate (25 mM), 1.5 mL of tannic acid (2.5 mM), and 1 mL of silver nitrate (25 mM) were used. The whole process was carried out at a constant temperature of 90  $^{\circ}$ C. Finally, Ag NPs were centrifuged and redispersed in 20 mL of deionized water.

### 2.3. Preparation of SERS Substrates of Au and Ag NPs

A silicon wafer (SW) with a surface area of 1 cm<sup>2</sup> was used to support metal NPs. First, a SW was washed with xylene (Sigma-Aldrich, 98%), acetone (Sigma-Aldrich, 98%), and ethanol (Sigma-Aldrich) for 10 min. Then, it was rinsed with deionized water and further dried in a muffle at 100  $^{\circ}$ C. Subsequently, a fixed volume of metal NPs ( $V_{NP}$ ) in solution was deposited on the wafer. The solvent present in the solution was evaporated using a tubular oven (Thermo Scientific, Lindberg Blue M) at 60  $^{\circ}$ C, under a nitrogen flow (0.2 mL/s) for 30 min. Finally, without further treatment, the SW with NPs on it was viewed under an electronic microscope. To fabricate various SS, a similar procedure was repeated by using  $V_{NP} = 50, 100, 150, 200,$  and 250  $\mu$ L of Au or Ag NP solution.

### 2.4. Deposition of T4 on Different Substrates

Initially, we measured the Raman signal of the T4 precursor, as follows: As obtained directly from the reagent bottle, T4 crystals were used to completely cover a SW (pretreated as detailed above). Then, the SW was put in the Raman equipment to be characterized. Separately, dilute solutions of T4 with concentrations from 10  $\mu$ M to 1 mM were also prepared. They were obtained from a mixture of methanol (Sigma-Aldrich, 98%) and deionized water (18.2 M $\Omega$  cm), at a ratio of 1:1 V:V. Afterward, 50  $\mu$ L of T4 dilute solution

was deposited on a nude SW (pretreated). The solvent was evaporated at 50 °C in a tubular oven with a nitrogen flow (0.5 mL/s) for 3 h. Finally, each sample was characterized by the Raman technique.

#### SERS Substrate Preparation

Once each SS was fabricated, as indicated in Section 2.3, 50 µL of T4 concentrations from pM to mM were deposited onto it. Afterward, the solvent was evaporated at 50 °C for 3 h in a tubular oven with a nitrogen flow (0.5 mL/s). Finally, each sample was characterized by the Raman technique. For each substrate, the Raman spectrum was the average response over ten spots on its surface.

#### 2.5. Equipment

A UV-Vis-NIR Agilent-Varian-Cary 5000 spectrophotometer was used to measure the absorbance spectra of the metal NP solutions.

To visualize the shape, size, and spatial distribution of metal NPs, on the SW, a JEOL scanning electron microscope (SEM) was used (model JSM 7800F) with a 5 keV voltage.

For all experiments, a HORIBA Jobin Yvon Micro-Raman LabRam HR was used to capture the Raman signal. The equipment has an OLYMPUS BX41 microscope with a magnification of 100×, to focus on the area under study. The samples were irradiated with a monochromatic He–Ne laser (632.8 nm and power of 6 mW). The capture time was 10 s for 5 cycles. No filters were used.

#### 2.6. Theoretical-Numerical Calculations

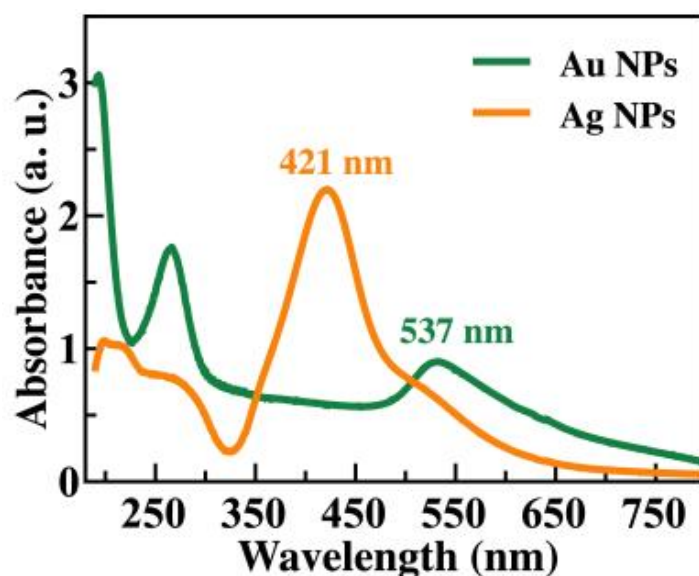
Theoretical-numerical modeling was performed by employing the discrete dipole approximation (DDA) under its free numerical implementation, named *ddscat* 7.0. Over the previous decades, DDA has been used to study the optical response of organic and inorganic materials. The dimensions of those materials span from angstroms to millimeters, and even centimeters. A list of targets includes nanotubes, nanoparticles, bacteria, red blood cells, and graphite grains [42–46].

There is a great variety of articles where the fundamentals of DDA have been exposed in great detail. In brief, DDA is a tool for solving Maxwell's equations by using a set of *N*-point dipoles to mimic the solid target. The induced dipoles radiated by an incident electromagnetic plane wave generate their own electric field. The coupled dipoles are related to the incident and induced fields through a 3 *N* complex equation system [41,47,48]. This approximation allows the modeling of optical response in the far (scattering, absorption, extinction, reflection, and transmission) and near (electric field in and close to the particle's surface) regimes.

After a study of convergence, we employed point dipoles of about  $2 \times 10^5$  to mimic each target. Extinction efficiencies and electric field were calculated for systems of 1 to 3 NPs of 50 nm in diameter, with a surface-to-surface separation distance of 1 nm. For the dielectric function of gold and silver, the finite size correction to the bulk material was considered because for this size the electronic confinement is not negligible [49].

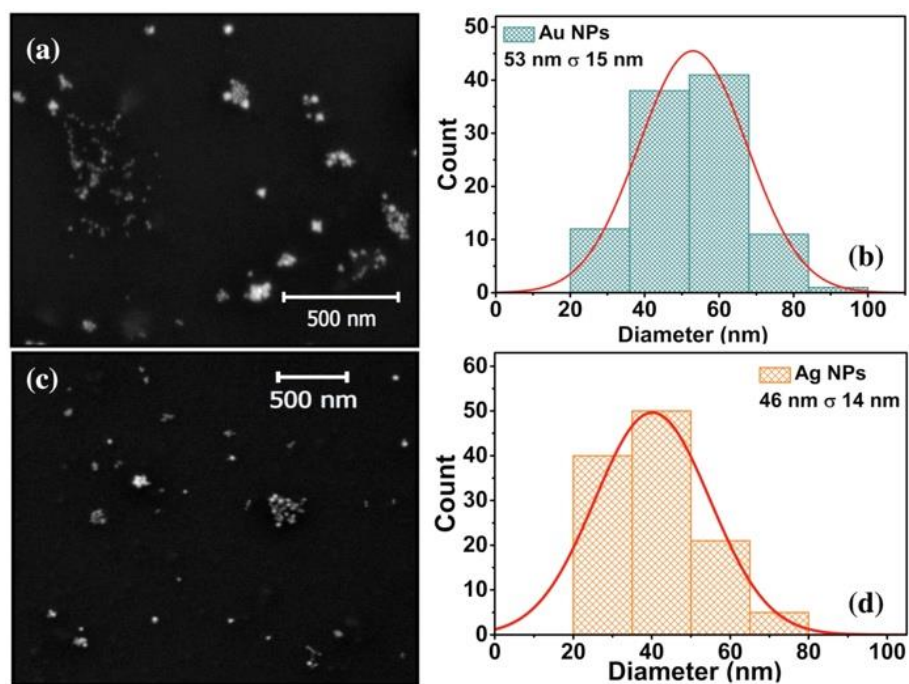
### 3. Results and Discussion

Figure 1 shows the absorbance spectra of the Au (green line) and Ag (orange line) NPs in solution. The band observed at 537 nm is an Au surface plasmon feature [50,51]. While the band located at 421 nm corresponds to the Ag NP localized surface plasmons. Moreover, in both spectra, there are two optical bands below 300 nm. The Ag NPs are assigned to the presence of tannic acid as the functionalizing agent (see Figure S1 in the Electronic Supplementary Material (ESM)) [41,52] and to the electronic interband transitions of silver [53]. In the case of the Au NP spectrum, the two bands observed correspond to L-ascorbic acid as the functionalizing agent (see Figure S2 in ESM) and the Au interband transitions [53].



**Figure 1.** Position of the surface plasmon resonance of Au (green line) and Ag (orange line) NPs in colloidal solution. Bands below 300 nm are the outcome of electronic interband transitions and optical excitations of functionalizing molecules.

Various SS were fabricated to deposit freely in a volume concentration of metal NPs ( $V_{NP} = 50, 100, 150, 200,$  and  $250 \mu\text{L}$ ) on a SW. SEM images of Au and Ag SS with a  $V_{NP} = 50 \mu\text{L}$  are shown in Figure 2a,c. Quasi-spherical single NPs and small clusters of them are distributed along the SW surface. The size distribution was determined from a sample of 150 NPs. The average size is  $53 \pm 15 \text{ nm}$  and  $46 \pm 14 \text{ nm}$  for Au and Ag NPs, respectively (see Figure 2b,d for the size distributions).



**Figure 2.** (a) SEM micrograph and (b) size distribution of Au NPs supported on a silicon wafer. Whereas (c,d) correspond to Ag NPs. Here, a  $V_{NP} = 50 \mu\text{L}$  was deposited on the SW.

Figure 3 shows the Raman signal of T4 crystals, where several bands are observed; the four most intense are located at  $216\text{ cm}^{-1}$ ,  $822\text{ cm}^{-1}$ ,  $1044\text{ cm}^{-1}$ , and  $1050\text{ cm}^{-1}$ . The first is associated with the planar bending vibrational mode of the C–C–I bonds, the second is designated to a ring deformation vibrational mode; the third and fourth bands are originated by a combination of stretching vibrations by the C–O and C–N bonds [54–56].

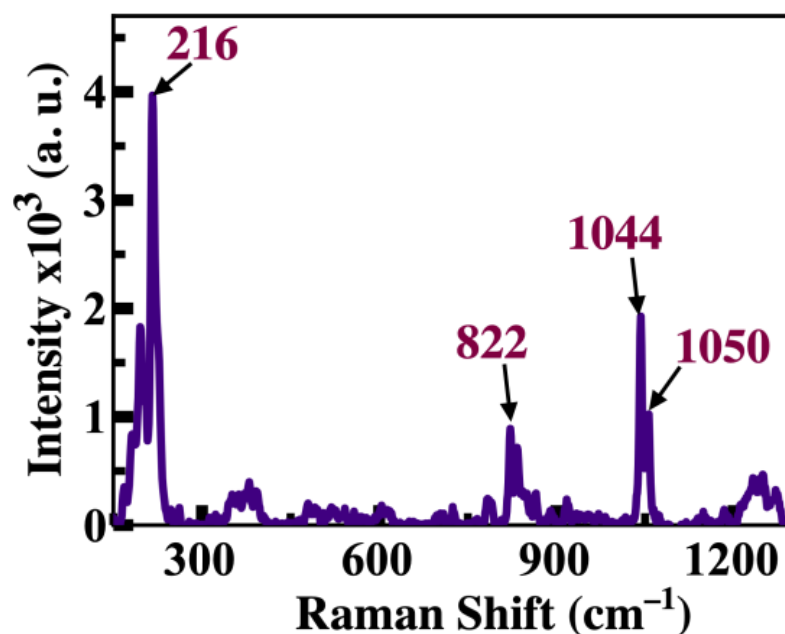
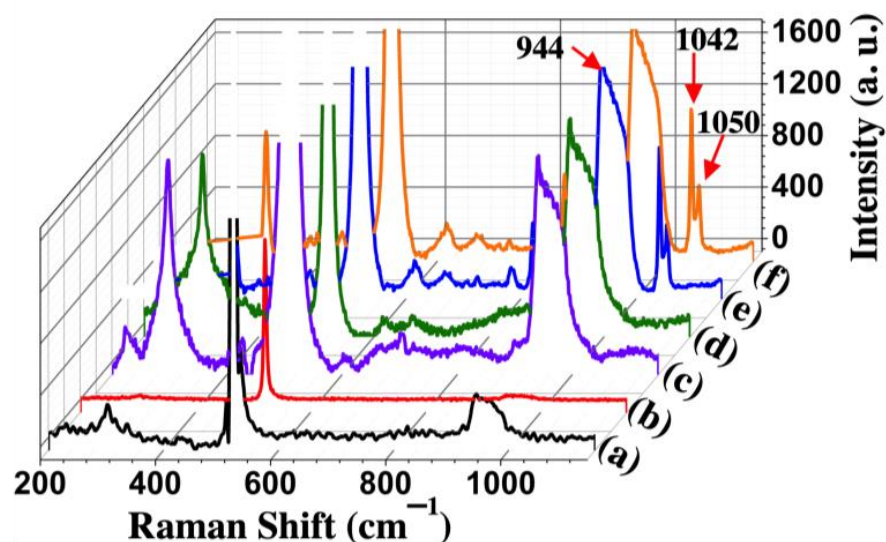


Figure 3. Raman spectrum of T4 crystals.

In Figure 4, we present the Raman spectra of (a) a nude SW (black line), (b) T4 deposited on a SW (red line), (c) Au NPs on a SW (purple line), (d) Ag NPs on a SW (green line), (e) T4 deposited on Au NPs (blue line), and (f) on Ag NPs (orange line). Both, in (e) and (f), the NPs were freely dropped off on the SW. Moreover, in all cases, the concentration of T4 was 1 mM. Here, the SS were prepared with a  $V_{NP} = 50\ \mu\text{L}$  (3 mM). In the silicon wafer spectrum, the three main bands located at  $300\text{ cm}^{-1}$ ,  $520\text{ cm}^{-1}$ , and  $944\text{ cm}^{-1}$  are observed. The first one corresponds to the acoustic transverse vibrational mode, and the other two to the optical transverse vibrational modes [57]. The silicon band at  $520\text{ cm}^{-1}$  is very intense and observable in all six spectra; therefore, we cut the intensity scale with the sole purpose of clearly showing the bands above  $800\text{ cm}^{-1}$ . In the red-line spectrum, no T4 band is distinguished because of the small molecule concentration being used (1 mM), the same happens for lower T4 concentrations (not shown here). Noticeably, the Raman intensity of the T4 bands is greatly increased because of the optical response by the metal NPs, specifically, by the bands located at  $216\text{ cm}^{-1}$ ,  $822\text{ cm}^{-1}$ ,  $1042\text{ cm}^{-1}$ , and  $1050\text{ cm}^{-1}$ , see blue and orange lines. As we can see, the sole presence of the functionalized metal NPs increases the intensity of the silicon bands (compare spectral lines (a) with (c) and (d)). The last result motivated us to trace the intensity of one Si band as the number of NPs deposited on the SW surface increases.

The Raman signal of SW with different Ag NP volumes,  $V_{NP}$ , was measured. We varied  $V_{NP}$  from 0 (nude SW) to  $250\ \mu\text{L}$ . Even using  $250\ \mu\text{L}$  of NPs did not cover the SW area 100% (see SEM images in Figure S3 in ESM). Figure 5 shows the Raman spectra around  $520\text{ cm}^{-1}$ . In essence, the band position remains unchanged. However, the intensity is notably modified. The band intensity when using  $50\ \mu\text{L}$  of Ag NPs is eight times that of the nude wafer. The inset demonstrates a non-linear decreasing relationship between the band intensity and the  $V_{NP}$ . As  $V_{NP}$  increases, more SW surface is covered by metal NPs; therefore, a decrement in the silicon band intensity is expected.



**Figure 4.** Raman spectrum of (a) SW (black line), (b) T4 at a concentration of 1 mM dropped on a SW (red line), (c) Au NPs on a SW (purple line), (d) Ag NPs on a SW (green line), (e) T4 on Au NPs (blue line), and (f) T4 on Ag NPs (orange line). (e,f) Measured on a SW with the same T4 concentration as in (b). Here, the SS were prepared with a  $V_{NP} = 50 \mu\text{L}$  (3 mM).

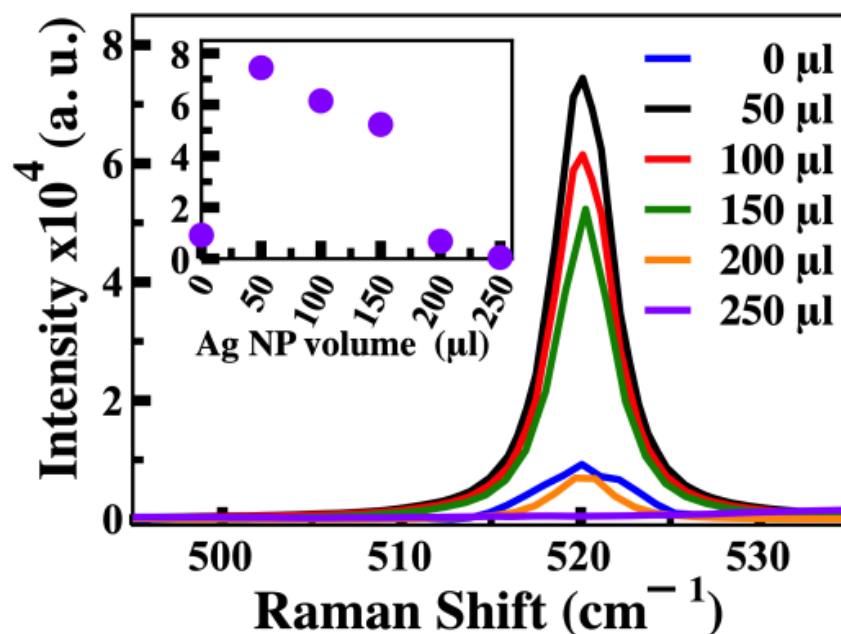


**Figure 5.** Raman signal intensity of the silicon band at  $520 \text{ cm}^{-1}$  for a SW covered by different amounts of Ag NPs ( $V_{NP} = 50, 100, 150, 200,$  and  $250 \mu\text{L}$ ).  $V_{NP} = 0 \mu\text{L}$  represents a nude SW. The purple dots in the inset shows the relationship between the Si band intensity at  $520 \text{ cm}^{-1}$  and the  $V_{NP}$  of Ag NPs.

To assess the T4 band that would be the best at determining the SERS enhancement factor (SERS-EF), we followed the following criteria: The T4 band at  $216 \text{ cm}^{-1}$  was discarded because of a slight overlap with the Si band around  $300 \text{ cm}^{-1}$ , see Figure 4 lines (a), (c), and (d). The band at  $822 \text{ cm}^{-1}$  was also dismissed because of its low intensity, making it untraceable at very low T4 concentrations. Therefore, the band located at  $1042 \text{ cm}^{-1}$  was the one chosen to determine the SERS-EF value at an excitation wavelength of 632 nm. Then, we varied the T4 concentration from mM down to pM.

SS fabricated with  $V_{NP} = 50 \mu\text{L}$  of Au or Ag NPs are suitable for sensing a T4 concentration of  $50 \mu\text{M}$  (Figure 6 panels (a) and (b)). On the other hand, when a SS fabricated with a  $V_{NP} = 250 \mu\text{L}$  is employed, the Raman signal is even more intense; consequently, lower T4 concentrations can be measured (panels (c) and (d) of Figure 6). The Ag SS offered a good performance since it detected a concentration of  $10 \text{ pM}$ . However, with Au, the lowest T4 concentration detected was  $1 \mu\text{M}$ . A larger  $V_{NP}$  means more metal NPs on the SW substrate; therefore, a larger signal intensity is expected because more T4 molecules would be in close vicinity to the plasmonic surfaces.

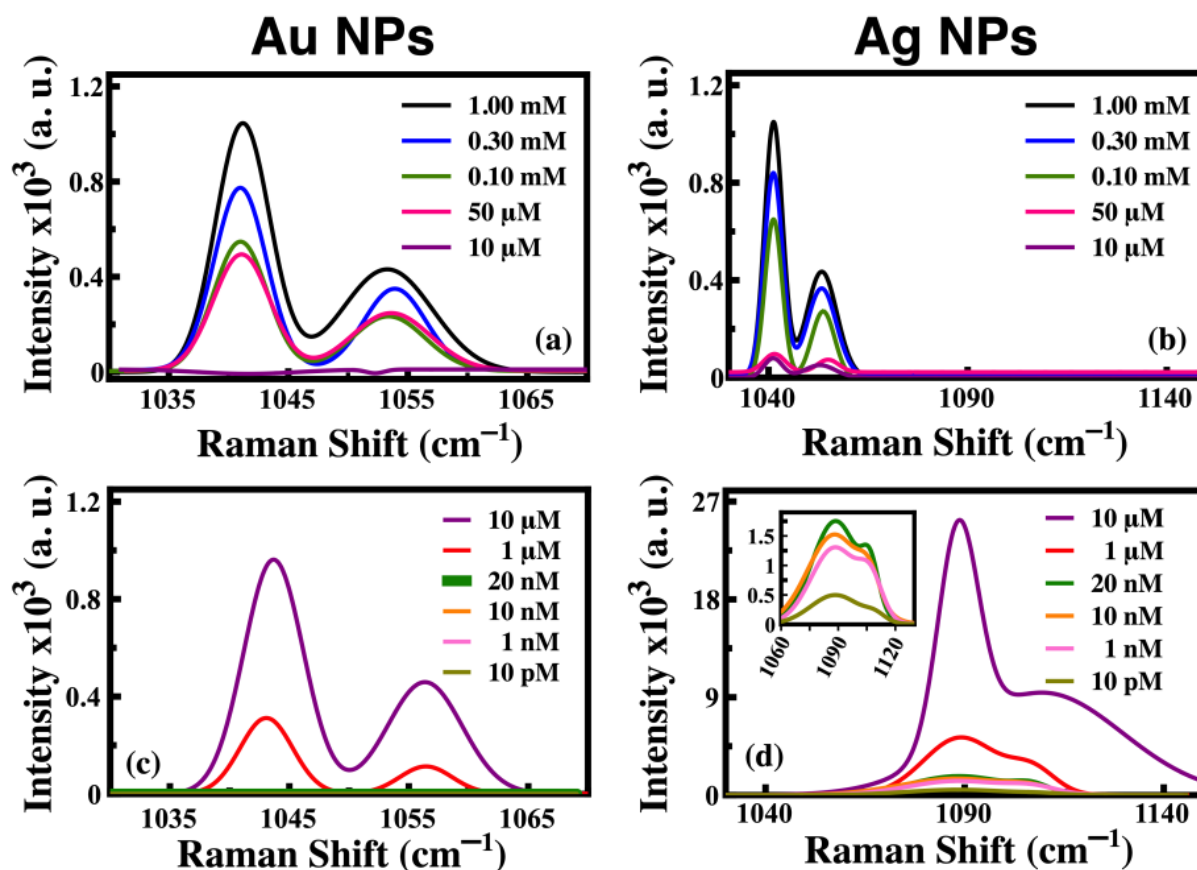


**Figure 6.** Raman spectra of the T4 bands, selected in this work, using Au and Ag as SS. T4 concentrations from pM to mM were monitored under an excitation wavelength of  $632 \text{ nm}$ . The Raman intensity shown in the upper panels was reached by using SS fabricated with  $V_{NP} = 50 \mu\text{L}$  and in the lower panels with  $V_{NP} = 250 \mu\text{L}$ .

In general, for a  $V_{NP}$  of fixed Au and Ag (see panels (a) and (b) or (c) and (d) of Figure 6), the intensity of the chosen band decreases and its position is unaltered as the T4 concentration decreases (note that the band at  $1050 \text{ cm}^{-1}$  changes in intensity and position for a fixed  $V_{NP}$ ). However, the position of the band is affected when the number of NPs on the silicon substrate changes; in other words, when  $V_{NP}$  changes, a frequency or wavenumber shift in SERS is promoted: Compare panel (a) with (c) or (b) with (d). Noticeably, while the shift for the Au SS is imperceptible (about  $2\text{--}3 \text{ cm}^{-1}$ ), the shift for Ag SS reaches tens of  $\text{cm}^{-1}$ . Particularly, the Ag SS with a low NP volume ( $V_{NP} = 50 \mu\text{L}$ ) has a band around  $1042 \text{ cm}^{-1}$ , for all high T4 concentrations. However, that band is displaced towards larger wave numbers ( $1088 \text{ cm}^{-1}$ ) for the Ag SS with a high NP volume ( $V_{NP} = 250 \mu\text{L}$ ), for all low T4 concentrations.

To elucidate the origin of the wavenumber shift in the SERS; we fixed the T4 concentration at  $10 \mu\text{M}$  and varied  $V_{NP}$  from  $50 \mu\text{L}$  to  $250 \mu\text{L}$ . In Figure 7, we present the Raman spectra of T4 measured on SW using different NP volumes. As the  $V_{NP}$  increases, the band

at  $1042\text{ cm}^{-1}$  moves toward the larger wave numbers (red dots in the right panel of Figure 7). Probably, the SERS frequency shift originates from the structural deformation of the analyte, as a consequence of the binding events because the loading of plasmonic nanoparticles increases, in addition to the possible charge transfer between the tannic acid functionalized Ag NP and the T4, or vice versa. Our assumptions are based on a similar frequency shift in SERS as observed in the other systems [58–62]. On the other hand, the best fit to the intensity- $V_{NP}$  relation (blue diamonds in the right panel of Figure 7) is a fourth-degree polynomial expressed by  $I(V_{NP}) = -2.87 \times 10^{-5} V_{NP}^4 + 0.02 V_{NP}^3 - 2.40 V_{NP}^2 + 94.25$ .

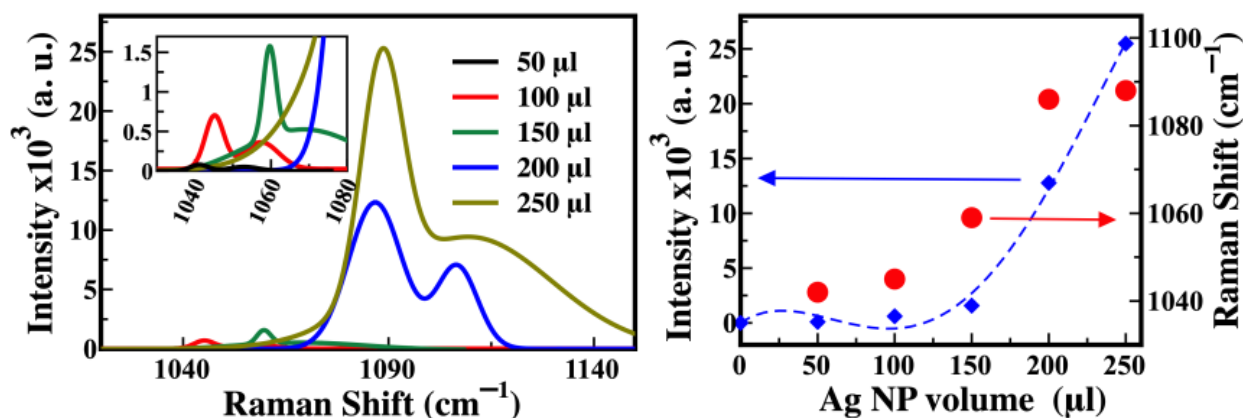


**Figure 7.** Measured Raman intensity of T4 molecules, at a fixed concentration of  $10\text{ }\mu\text{M}$ , on various SS. Each SS is a SW with a specific Ag NP volume ( $V_{NP}$  from 50 to 250  $\mu\text{L}$ ). As  $V_{NP}$  increases, the band originated by stretching vibrations of C–O and C–N bonds is displaced from  $1042\text{ cm}^{-1}$  to  $1088\text{ cm}^{-1}$  (red dots in the right panel). Furthermore, its intensity increases, thereby obeying a fourth-degree polynomial relationship with  $V_{NP}$  (blue diamonds and dashed blue line in the right panel).

Next, to determine SERS-EF, the following equation was used:

$$\text{SERS-EF} = \frac{(I_{\text{SERS}} \cdot N_{\text{Raman}})}{(I_{\text{Raman}} \cdot N_{\text{SERS}})} \quad (1)$$

$I_{\text{SERS}}$  and  $I_{\text{Raman}}$  are the Raman band intensities of the T4 supported on a SS and a nude SW (without the metal NPs), respectively.  $N_{\text{Raman}}$  and  $N_{\text{SERS}}$  are the excited T4 molecules on the SW without and with metal NPs, respectively.  $N_{\text{Raman}}$  and  $N_{\text{SERS}}$  were determined by considering the area occupied by each molecule (see Figure S4 in ESM), the number of molecules within the laser spot area ( $12.5 \times 10^7\text{ nm}^2$ ), and in the case of SS, the number of molecules on the metal NPs (see Tables S1 and S2 in ESM). It is relevant to mention that a 3 nm thick layer of T4 was considered on the surface of the NPs because the intensity of the electric field begins to decrease remarkably for distances beyond 3 nm from the metal surface (see Figure S5 in ESM).

We focused on the band intensity at  $1044\text{ cm}^{-1}$  to estimate the SERS-EF using Equation (1) for the different T4 concentrations. Table 1 contains the  $I_{\text{Raman}}$ ,  $I_{\text{SERS}}$ ,  $N_{\text{Raman}}$ ,  $N_{\text{SERS}}$ , and SERS-EF for each concentration and each metal SS. The T4 concentration was varied between 1 mM and 1 pM. The first six lowest T4 concentrations were tested on the  $V_{NP} = 250\text{ }\mu\text{L}$  SS. The last five highest T4 concentrations were tested on the  $V_{NP} = 50\text{ }\mu\text{L}$  SS. For all SS, the SERS-EF behaved according to the T4 concentration. However, the Ag NP SS demonstrated a larger sensitivity than the Au NP SS. The minimum concentration detected using Au was 1  $\mu\text{M}$ , whereas with Ag, it was 10 pM. The detected value with the Ag SERS platform was well below the indicative values of a healthy human body ( $\approx 64\text{ nM}$  [63]); therefore, the visualization of this platform is a candidate for detecting hypothyroidism issues.

**Table 1.**  $I_{\text{Raman}}$ ,  $I_{\text{SERS}}$ ,  $N_{\text{Raman}}$ , and  $N_{\text{SERS}}$ , at different T4 concentrations with Au and Ag SS. SERS-EF was calculated using Equation (1) and intensities of the band  $1044\text{ cm}^{-1}$ . The first six lower T4 concentrations were tested on  $V_{\text{NP}} = 250\text{ }\mu\text{L}$  SS. The last five higher T4 concentrations were tested on  $V_{\text{NP}} = 50\text{ }\mu\text{L}$  SS.

Au NPs					
T4 Concentration	$I_{\text{Raman}}$	$I_{\text{SERS}}$	$N_{\text{Raman}}$	$N_{\text{SERS}}$	SERS-EF
10 pM	1	1	16.2	$3.06 \times 10^{-8}$	$5.29 \times 10^8$
1 nM	1	1	$1.62 \times 10^3$	$3.06 \times 10^{-6}$	$5.29 \times 10^8$
10 nM	1	1	$1.62 \times 10^4$	$3.06 \times 10^{-5}$	$5.29 \times 10^8$
20 nM	1	1	$3.24 \times 10^4$	$6.13 \times 10^{-5}$	$5.29 \times 10^8$
1 $\mu\text{M}$	1	312	$1.62 \times 10^6$	$3.05 \times 10^{-3}$	$1.65 \times 10^{10}$
10 $\mu\text{M}$	1	962	$1.61 \times 10^7$	$3.05 \times 10^{-1}$	$5.08 \times 10^{10}$
10 $\mu\text{M}$	1	1	$3.77 \times 10^6$	$2.56 \times 10^6$	$1.18 \times 10^2$
0.05 mM	1	478	$1.88 \times 10^8$	$2.56 \times 10^6$	$1.20 \times 10^4$
0.10 mM	1	516	$3.78 \times 10^8$	$2.56 \times 10^6$	$5.49 \times 10^4$
0.30 mM	1	739	$1.13 \times 10^9$	$2.56 \times 10^6$	$2.68 \times 10^5$
1.00 mM	1	1022	$3.78 \times 10^9$	$2.56 \times 10^6$	$2.20 \times 10^6$
Ag NPs					
T4 Concentration	$I_{\text{Raman}}$	$I_{\text{SERS}}$	$N_{\text{Raman}}$	$N_{\text{SERS}}$	SERS-EF
10 pM	1	518	16.2	$3.38 \times 10^{-7}$	$2.48 \times 10^9$
1 nM	1	1318	$1.62 \times 10^3$	$3.38 \times 10^{-5}$	$6.30 \times 10^9$
10 nM	1	1538	$1.62 \times 10^4$	$3.38 \times 10^{-4}$	$7.35 \times 10^9$
20 nM	1	1787	$3.24 \times 10^4$	$6.77 \times 10^{-4}$	$8.54 \times 10^9$
1 $\mu\text{M}$	1	5458	$1.62 \times 10^6$	$3.38 \times 10^{-2}$	$2.61 \times 10^{10}$
10 $\mu\text{M}$	1	25,481	$1.61 \times 10^7$	3.37	$1.22 \times 10^{11}$
10 $\mu\text{M}$	1	91	$3.78 \times 10^7$	$8.99 \times 10^5$	$3.82 \times 10^3$
0.05 mM	1	79	$1.88 \times 10^8$	$8.99 \times 10^5$	$1.66 \times 10^4$
0.10 mM	1	681	$3.78 \times 10^8$	$8.99 \times 10^5$	$2.86 \times 10^5$
0.30 mM	1	870	$1.13 \times 10^9$	$8.99 \times 10^5$	$1.10 \times 10^6$
1.00 mM	1	1073	$3.78 \times 10^9$	$8.99 \times 10^5$	$4.52 \times 10^6$

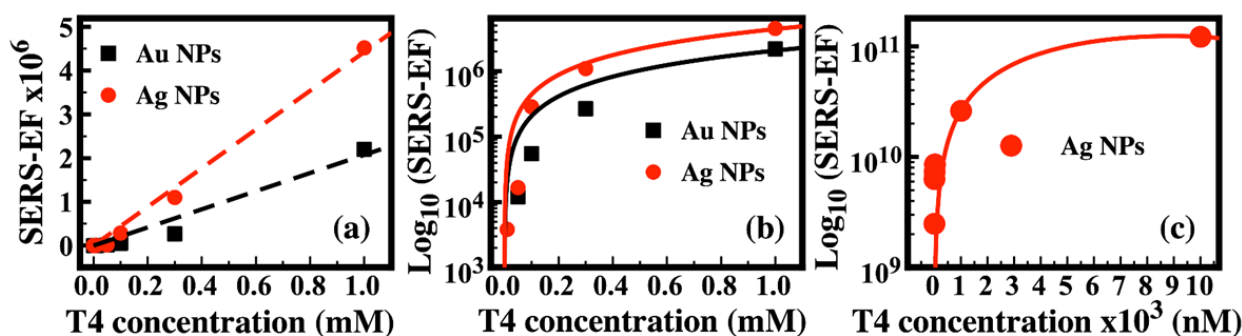
As a general behavior, SERS-EF follows an increasing trend as the T4 concentration increases, see Figure 8. In the case of the Au and Ag 50  $\mu\text{L}$  SS, a linear fitting with a correlation coefficient of 0.96 for Au and 0.99 for Ag was obtained (Figure 8a). Furthermore, using the Ag SS, a higher SERS-EF is reached compared to Au SS, which was verified by comparing the slope values. A logarithmic scale is shown in Figure 8b to appreciate the behavior of SERS-EF since it diminishes by orders of magnitude as the concentration decreases.

In the case of the Au 250  $\mu\text{L}$  SS, the SERS-EF for analyte concentrations from 10  $\mu\text{M}$  to 1  $\mu\text{M}$  did not result in great variations when the estimated values went from  $5.08 \times 10^{10}$  to  $1.65 \times 10^{10}$  (see Table 1, shaded files). For lower concentrations, the signal was so weak that a trace was impossible.

On the other hand, with the Ag 250  $\mu\text{L}$  SS, it was feasible to track the intensity for T4 concentrations from 10  $\mu\text{M}$  to 10 pM, as it was accompanied by a decrease in the SERS-EF changes from  $10^{11}$  to  $10^9$  (see Table 1 and Figure 8c). The best fitting for the relationship  $\text{Log}_{10}(\text{SERS-EF})$  vs. T4 concentration is a second-order polynomial with a correlation coefficient of 0.99.

The results indicate that our Ag SERS platform is more sensitive to detecting T4 than other techniques based on chromatography and mass spectroscopy [13]. For example, Luna et al. reported a LOD of 260 pM. Recently, Karami and colleagues used magnetic nanoparticles, electrochemical methods, and immunoassay analysis to reach a LOD of 3 pM for T4 [20]. Although their sensitivity is similar to that of our platform, their methodology is more complex. On the other hand, Orlov et al. reported FT4 detection by using magnetic NPs and immunoassays with a LOD of 20 fM [16]. Their work motivates us and the next

step in our research is to optimize the Ag SS with a suitable  $V_{NP}$  to get the maximum SERS-EF, expecting to reach a LOD of fM orders.



SERS-EF = B (T4 Concentration) + A				
Sample	Interception (A)	Slope (B)	Adj. R-Square ( $R^2$ )	
Au NP SS (50 $\mu$ L)	0.0	$2.07 \times 10^6$	0.96	
Ag NP SS (50 $\mu$ L)	0.0	$4.90 \times 10^6$	0.99	
SERS-EF = A + B <sub>1</sub> (T4 Concentration) + B <sub>2</sub> (T4 Concentration) <sup>2</sup>				
Sample	Interception (A)	B <sub>1</sub>	B <sub>2</sub>	Adj. R-Square ( $R^2$ )
Ag NP SS (250 $\mu$ L)	0.0	$2.80 \times 10^7$	$-1.57 \times 10^3$	0.99

**Figure 8.** Plot of SERS-EF vs. T4 concentration (a) and  $\text{Log}_{10}$  (SERS-EF) vs. T4 concentration using NP SS with  $V_{NP} = 50 \mu\text{L}$  (b), and with  $V_{NP} = 250 \mu\text{L}$  (c).

In the case of SS with  $V_{NP} = 50 \mu\text{L}$ , single NPs far away one each other, quasi-spherical clusters made with few NPs, and semi-linear arrays of NPs in random orientations are observed on the SW surface (see SEM images of Figure 2). Then, the SERS-EF, determined indirectly by experimental measurement, is an average of the SERS-EF promoted by each configuration. We numerically estimated the SERS-EF of some configurations under an excitation wavelength equal to that of the SERS experiments.

For the determination of the SERS-EF, we used the approximation of  $|E|^4$  provided by the following equation:

$$\text{SERS-EF} \approx \frac{|E_{\text{loc}}(\omega_{\text{exc}})|^2 |E_{\text{loc}}(\omega_{\text{Raman}})|^2}{|E_{\text{inc}}|^2 |E_{\text{inc}}|^2} \approx \frac{|E_{\text{loc}}(\omega_{\text{exc}})|^4}{|E_{\text{inc}}|^4}, \quad (2)$$

where  $E_{\text{loc}}$  and  $E_{\text{inc}}$  are the local and incident electric fields, respectively, evaluated at the position where the molecule stands.  $\omega_{\text{exc}}$  is the excitation frequency and  $\omega_{\text{Raman}}$  is the Stokes shift Raman frequency of the molecule [26].

Figure 9a shows near-electric field images of a single NP, a triangular cluster, and three NPs aligned. For an isolated Au NP, the hot spots near its surface contributed to an enhancement factor of  $5.2 \times 10^2$ . In the case of the triangular agglomerate, the hot spot is located between the two NPs whose equator is parallel to the  $Y$ -axis; its SERS-EF is around  $8.1 \times 10^5$ . However, when the three Au NPs are aligned, the hot spots are in the interparticle gaps with a SERS-EF of  $2.4 \times 10^7$ . The optical band of a single Au NP is at 512 nm, while the triangular cluster and linear agglomerate optical band are located at 574 and 590 nm, respectively (Figure 9b). The excitation wavelength has been indicated with a dashed line. The silicon substrate effect has not been considered, if so, the spectra would be red-shifted compared to those observed in Figure 9b. Then, an in-resonance condition is almost fulfilled. D.D. Li et al. [64] studied the optical efficiency of linear and non-linear agglomerates of 20 nm Au NPs. They found that the linear agglomerates

present two surface plasmon resonances, one longitudinal and one transverse, while the quasi-spherical agglomerates present a very broad principal resonance. Our results are well matched with those. In our case, the incident wave has a polarization state in the Y-axis (parallel to the equator of the NPs), which prefers the longitudinal plasmon band, meaning that the transverse plasmon band is not appreciated.

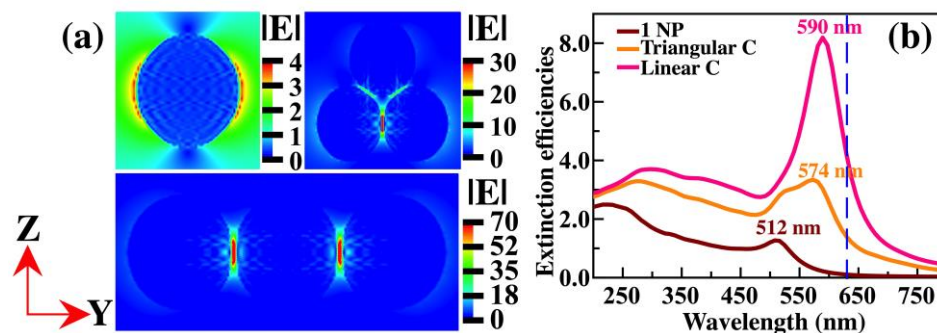


**Figure 9.** (a) Electric field magnitude and (b) extinction efficiency of a single NP, a triangular cluster of NPs, and three NPs aligned. All Au NPs are 50 nm in diameter; the surface-to-surface separation distance is 1 nm. The polarization state of the incident wave is parallel to the equator of the NPs (Y-axis) with a traveling direction along the X-axis. In all cases, the incident wavelength is 632 nm (position indicated with a dashed line), and air is the surrounding medium.

In the case of Ag NPs, the image of the electric field magnitude (Figure 10a) is very similar to that of the Au NPs, except that the scale is different. The SERS-EF in the hot spots is about  $1.5 \times 10^2$ ,  $3.9 \times 10^5$ , and  $2.5 \times 10^6$  for the single NP, triangular cluster, and linear array, respectively. The orders of magnitude are similar to those obtained by Au. The plasmonic bands of all three configurations are shown in Figure 10b. We observed that all three systems when in air, are out-of-resonance at an excitation wavelength of 632 nm. However, a red-shift in the spectrum is expected when the silicon substrate is included in the simulations, thereby making it closer to the in-resonance condition.

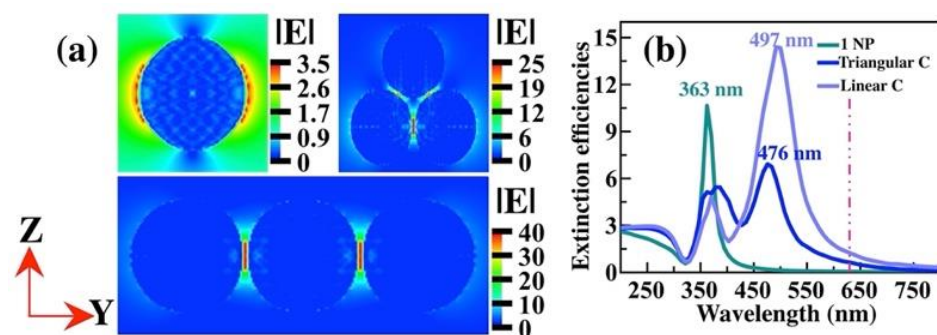


**Figure 10.** (a) Electric field magnitude and (b) extinction efficiencies of a single NP, a triangular cluster of NPs, and three NPs aligned. All Ag NPs are 50 nm in diameter; the surface-to-surface separation distance is 1 nm. The polarization state of the incident wave is parallel to the equator of the NPs (Y axis) with a traveling direction along the X axis. In all cases, the incident wavelength is 632 nm (position indicated with a dashed line), and air is the surrounding medium.

#### 4. Conclusions

In this work, we synthesized functional Au and Ag NPs with ascorbic and tannic acid, respectively. They have a spherical shape and a diameter of about 50 nm. They were deposited on silicon wafers and tested as SERS substrates (SS) for T4 detection. SS were fabricated with different loads of metal NPs, i.e., with volume concentrations ( $V_{NPs}$ ) from 50  $\mu\text{L}$  (3 mM) to 250  $\mu\text{L}$ .

We focused on the T4 band at  $1044\text{ cm}^{-1}$  and tracked its intensity and position at concentrations from 10 pM to 1 mM. For all SS, the band intensity decreases as the T4 concentration decreases. In the case of the Au SS with the highest load of NPs ( $V_{NP} = 250\text{ }\mu\text{L}$ ), the minimum concentration detected was 1  $\mu\text{M}$ . The Ag NP SS with the same load demonstrated a better performance by detecting a concentration of 10 pM. Therefore, our label-free Ag NP SS visualization can be used as a candidate to detect hypothyroidism or other health issues, where detection at low concentrations is a requirement. In the next stage of our research, an optimization study to determine the suitable  $V_{NP}$  to get the highest SERS signal is on the list of things to do.

On the other hand, for a fixed T4 concentration (1  $\mu\text{M}$ ), a wave number shift in SERS is observed as the load of NPs increases. Particularly, when the Ag SS with the minimum ( $V_{NP} = 50\text{ }\mu\text{L}$ ) and maximum ( $V_{NP} = 250\text{ }\mu\text{L}$ ) load of NPs were implemented, the band at  $1044\text{ cm}^{-1}$  shifted till  $1088\text{ cm}^{-1}$ , a shift of about  $44\text{ cm}^{-1}$ . In the case of the Au SS, the same band only shifted two to three  $\text{cm}^{-1}$ . The shift could be originated, in part, by a possible charge transfer from the T4 molecule to the functionalized NP, or vice versa, in addition to T4 structural deformations as a consequence of binding events when the loading of plasmonic nanoparticles increases. However, further studies must be realized to confirm our assumptions.

The SERS enhancement factor was estimated from a detailed analysis that included the spatial distribution of NPs on the silicon wafer surface, the size of the T4 molecule, the number of excited molecules in Raman and SERS conditions, and other experimental factors. In the case of the Ag SS with 250  $\mu\text{L}$  of NPs, a SERS-EF of  $10^9$  is suitable for detecting a T4 concentration of 10 pM.

For the SS with the lowest load of NPs, the spatial distribution of the NPs on the silicon wafer includes mainly single NPs, which are far away one each other, quasi-spherical clusters made with few NPs, and semi-linear arrays of NPs in random orientations. Then, we performed numerical simulations to determine the position and intensity of the hot spots at an excitation wavelength equal to the SERS experiment, 632 nm. We concluded that the hot spots at the interparticle gaps in a linear array of three NPs are more intense than for an isolated NP or a triangular cluster. Furthermore, from the calculation of the extinction efficiency, we can deduce that the Au NPs in the SS are in resonance at a wavelength of 632 nm. However, a resonance condition is not completely satisfied in Ag NP SS.

Finally, we believe the combination of our SERS platform and immunoassay analysis could be an interesting alternative to provide a method that offers good sensitivity and selectivity for point-of-care implementations.

**Supplementary Materials:** The following supporting information can be downloaded at: <https://www.mdpi.com/article/10.3390/chemosensors11100516/s1>, Figure S1: The left panel shows a SEM image of Ag NPs with a volume concentration ( $V_{NP}$ ) of 250  $\mu\text{L}$  at  $\times 160,000$  magnification. The presence of the functionalizing agent (tannic acid) surrounding the Ag NPs is seen as a transparent layer. The right panel shows the Raman spectrum of Ag NPs; Figure S2: Absorbance spectra of the colloidal solution of Au NPs; Figure S3: The left panel shows the amount of Ag NPs deposited on a section of Si wafer with a volume of 50  $\mu\text{L}$ . In the right panel, a volume of 250  $\mu\text{L}$  of Ag NPs was used. For comparative purposes, an area of the wafer of the same size ( $2.7\text{ }\mu\text{m} \times 3.6\text{ }\mu\text{m}$ ) is shown in both panels. The area shown is smaller than the laser spot area ( $12.56\text{ }\mu\text{m}^2$ ); Figure S4: Image of the thyroxine molecule inside a rectangular prism; Figure S5: Near electric field intensity image of an Au NP of 50 nm of diameter and plot of the mean  $|E|^4$  with increasing distance from the Au NP surface; Figure S6: SEM micrograph at a magnification of  $\times 15,000$  of the SERS substrate of (a) Au NPs and (b) Ag NPs; Table S1: Molecule concentration of T4, the total number of molecules in each T4 solution concentration, number of molecule-layers on the Si wafer, and the total thickness of the multi-layer array, and  $N_{\text{Raman}}$  value; Table S2: Values used to estimate the total metal area occupied by the NP that is under the laser spot.

**Author Contributions:** Conceptualization, E.S.-M. and A.L.G.; methodology, E.S.-M. and A.L.G.; numerical simulation, P.D.L.P. and A.L.G.; validation, P.D.L.P., E.S.-M. and A.L.G.; formal analysis, P.D.L.P., E.S.-M. and A.L.G.; investigation, P.D.L.P., E.S.-M. and A.L.G.; resources, E.S.-M. and A.L.G.; writing—original draft preparation, P.D.L.P. and A.L.G.; writing—review and editing, P.D.L.P., E.S.-M. and A.L.G.; funding acquisition, E.S.-M. and A.L.G. All authors have read and agreed to the published version of the manuscript.

**Funding:** This research was funded by Vicerrectoría de Investigación y Estudios de Posgrado, Benemérita Universidad Autónoma de Puebla, grant number 100504244-VIEP2023 and 100409188-VIEP2023.

**Institutional Review Board Statement:** Not applicable.

**Informed Consent Statement:** Not applicable.

**Data Availability Statement:** The original data presented in this study are available by further request to any of the authors.

**Acknowledgments:** P. de León thanks CONACYT for the doctorate student grant No. 330633 and the postdoctoral fellowship. A. L. González and E. Sanchez-Mora thank the VIEP-BUAP for the financial support.

**Conflicts of Interest:** The authors declare no conflict of interest.

## References

- Hiller-Sturmhöfel, S.; Bartke, A. The endocrine system: An overview. *Alcohol Health Res. World* **1998**, *22*, 153–164.
- Silva, J.F.; Ocarino, N.M.; Serakides, R. Thyroid hormones and female reproduction. *Biol. Reprod.* **2018**, *99*, 907–921. [[CrossRef](#)]
- Shokripour, M.; Imanieh, M.H.; Garayemi, S.; Omidifar, N.; Shirazi Yeganeh, B.; Althabhawee, F. Thyroid stimulating hormone, T3 and T4 population-based reference range and children prevalence of thyroid dysfunction: First report from South of Iran. *Iran J. Pathol.* **2022**, *17*, 427–434. [[CrossRef](#)] [[PubMed](#)]
- Thumvijit, T.; Supawat, B.; Wattanapongpitak, S.; Kothan, S.; Tungjai, M. Effect of iodinated radiographic contrast media on radioimmunoassay for measuring thyroid hormones. *Appl. Radiat. Isot.* **2022**, *185*, 110261. [[CrossRef](#)]
- UCLA. Health Endocrine Surgery Normal Thyroid Hormone LEVELS. Available online: <https://www.uclahealth.org/medical-services/surgery/endocrine-surgery/conditions-treated/thyroid/normal-thyroid-hormone-levels> (accessed on 10 July 2023).
- Martino, E.; Bambini, G.; Bartalena, L.; Mammoli, C.; Aghni-Lombardi, F.; Baschierli, L.; Pinchera, A. Human serum thyrotrophin measurement by ultrasensitive immunoradiometric assay as a first-line test in the evaluation of thyroid function. *Clin. Endocrinol.* **1986**, *24*, 141–148. [[CrossRef](#)]
- Fritz, K.S.; Wilcox, R.B.; Nelson, J.C. A Direct free thyroxine (T4) immunoassay with the characteristics of a total T4 immunoassay. *Clin. Chem.* **2007**, *53*, 911–915. [[CrossRef](#)] [[PubMed](#)]
- Ross, D.S. Serum thyroid-stimulating hormone measurement for assessment of thyroid function and disease. *Endocrinol. Metab. Clin. N. Am.* **2001**, *30*, 245–264. [[CrossRef](#)] [[PubMed](#)]
- Maes, M.; Meltzer, H.Y.; Cisyns, P.; Suy, E.; Schotte, C. An evaluation of basal hypothalamic-pituitary-thyroid axis function in depression: Results of a large-scaled and controlled study. *Psychoneuroendocrinology* **1993**, *18*, 607–620. [[CrossRef](#)] [[PubMed](#)]
- Neu, V.; Bielow, C.; Gostomski, I.; Wintringer, R.; Braun, R.; Reinert, K.; Schneider, P.; Stuppner, H.; Huber, C.G. Rapid and comprehensive impurity profiling of synthetic thyroxine by ultrahigh-performance liquid chromatography–high-resolution mass spectrometry. *Anal. Chem.* **2013**, *85*, 3309–3317. [[CrossRef](#)]
- Ackermans, M.T.; Klieverik, L.P.; Ringeling, P.; Endert, E.; Kalsbeek, A.; Fliers, E. An online solid-phase extraction–liquid chromatography–tandem mass spectrometry method to study the presence of thyronamines in plasma and tissue and their putative conversion from <sup>13</sup>C<sub>6</sub>-thyroxine. *J. Endocrinol.* **2010**, *206*, 327–334. [[CrossRef](#)]
- Ackermans, M.T.; Kettelarij-Haas, Y.; Boelen, A.; Endert, E. Determination of thyroid hormones and their metabolites in tissue using SPE UPLC-tandem MS. *Biomed. Chromatogr.* **2012**, *26*, 485–490. [[CrossRef](#)] [[PubMed](#)]
- Luna, L.G.; Coady, K.; McFadden, J.R.; Markham, D.A.; Bartels, M.J. Quantification of total thyroxine in plasma from xenopus laevis. *J. Anal. Toxicol.* **2013**, *37*, 326–336. [[CrossRef](#)] [[PubMed](#)]
- Kunisue, T.; Fisher, J.W.; Fatuyi, B.; Kannan, K. A method for the analysis of six thyroid hormones in thyroid gland by liquid chromatography–tandem mass spectrometry. *J. Chromatogr. B* **2010**, *878*, 1725–1730. [[CrossRef](#)] [[PubMed](#)]
- Kunisue, T.; Fisher, J.W.; Fatuyi, B.; Kannan, K. Determination of six thyroid hormones in the brain and thyroid gland using isotope-dilution liquid Chromatography/Tandem Mass Spectrometry. *Anal. Chem.* **2011**, *83*, 417–424. [[CrossRef](#)] [[PubMed](#)]
- Orlov, A.V.; Znoyko, S.L.; Pushkarev, A.V.; Mochalova, E.N.; Guteneva, N.V.; Lunin, A.V.; Nikitin, M.P.; Nikitin, P.I. Data on characterization and validation of assays for ultrasensitive quantitative detection of small molecules: Determination of free thyroxine with magnetic and interferometric methods. *Data Br.* **2018**, *21*, 1603–1611. [[CrossRef](#)]
- Bikkarolla, S.K.; McNamee, S.E.; Vance, P.; McLaughlin, J. High-sensitive detection and quantitative analysis of thyroid-stimulating hormone using gold-nanoshell-based lateral flow immunoassay device. *Biosensors* **2022**, *12*, 182. [[CrossRef](#)]

18. Kim, K.; Han, D.K.; Choi, N.; Kim, S.H.; Joung, Y.; Kim, K.; Ho, N.T.; Joo, S.W.; Choo, J. Surface-enhanced Raman scattering-based dual-flow lateral flow assay sensor for the ultrasensitive detection of the thyroid-stimulating hormone. *Anal. Chem.* **2021**, *93*, 6673–6681. [[CrossRef](#)]
19. David, M.; Serban, A.; Enache, T.E.; Florescu, M. Electrochemical quantification of levothyroxine at disposable screen-printed electrodes. *J. Electroanal. Chem.* **2022**, *911*, 116240. [[CrossRef](#)]
20. Karim, P.; Gholamin, D.; Johari-Ahar, M. Electrochemical immunoassay for one-pot detection of thyroxine (T4) and thyroid-stimulating hormone (TSH) using magnetic and Janus nanoparticles. *Anal. Bioanal. Chem.* **2023**, *415*, 4741–4751. [[CrossRef](#)]
21. Saxena, R.; Srivastava, S. A sensitive and one-step quantification of thyroid stimulating hormone using nanobiosensor. *Mater. Today Proc.* **2019**, *18*, 1351–1357. [[CrossRef](#)]
22. Zheng, P.; Wu, L.; Raj, P.; Mizutani, T.; Szabo, M.; Hanson, W.A.; Barman, I. A dual-modal single-antibody plasmonic spectro-immunoassay for detection of small molecules. *Small* **2022**, *18*, 2200090. [[CrossRef](#)] [[PubMed](#)]
23. Huang, Y.; Zhao, S.; Shi, M.; Liu, Y.M. Chemiluminescent immunoassay of thyroxine enhanced by microchip electrophoresis. *Anal Biochem.* **2010**, *399*, 72–77. [[CrossRef](#)]
24. Mu, X.; Li, S.; Lu, X.; Zhao, S. CE with chemiluminescence detection for the determination of thyroxine in human serum. *Electrophoresis* **2014**, *35*, 962–966. [[CrossRef](#)]
25. Mradula; Raj, R.; Devi, S.; Mishra, S. Antibody-labeled gold nanoparticles bases immunosensor for the detection of thyroxine hormone. *Anal. Sci.* **2019**, *63*, 799–806.
26. Ru, E.L.; Etchegoin, P. *Principles of Surface-Enhanced Raman Spectroscopy*; Elsevier: Oxford, UK, 2009.
27. Wang, Z.; Zong, S.; Wu, L.; Zhu, D.; Cui, Y. SERS-activated platforms for immunoassay: Probes, encoding methods, and applications. *Chem. Rev.* **2017**, *117*, 7910–7963. [[CrossRef](#)]
28. Doering, W.E.; Piotti, M.E.; Natan, M.J.; Freeman, G. SERS as a foundation for nanoscale optically detected biological labels. *Adv. Mater.* **2007**, *19*, 3100–3108. [[CrossRef](#)]
29. Liang, J.; Liu, H.; Lan, C.; Fu, Q.; Huang, C.; Luo, Z.; Jiang, T.; Tang, Y. Silver nanoparticles enhanced Raman scattering-based lateral flow immunoassays for ultra-sensitive detection of the heavy metal chromium. *Nanotechnology* **2014**, *25*, 495501. [[CrossRef](#)] [[PubMed](#)]
30. Liang, X.; Miao, X.; Xiao, W.; Ye, Q.; Wang, S.; Lin, J.; Li, C.; Huang, Z. Filter-membrane-based ultrafiltration coupled with surface-enhanced Raman spectroscopy for potential differentiation of benign and malignant thyroid tumors from blood plasma. *Int. J. Nanomed.* **2020**, *15*, 2303–2314. [[CrossRef](#)]
31. Wang, R.; Chon, H.; Lee, S.; Cheng, Z.; Hong, S.H.; Yoon, Y.H.; Choo, J. Highly sensitive detection of hormone estradiol E2 using SERS-based immunoassays for the clinical diagnosis of precocious puberty. *ACS Appl. Mater. Interfaces* **2016**, *8*, 10665–10672. [[CrossRef](#)] [[PubMed](#)]
32. Choi, S.; Hwang, J.; Lee, S.; Lim, D.W.; Joo, H.; Choo, J. Quantitative analysis of thyroid stimulating hormone (TSH) using SERS-based lateral flow immunoassay. *Sens. Actuators B Chem.* **2017**, *240*, 358–364. [[CrossRef](#)]
33. Kim, S.M.; Lee, T.; Gil, Y.G.; Kim, G.H.; Park, C.; Jang, H.; Min, J. Fabrication of bioprobe self-assembled on Au-Te nanoworm structure for SERS biosensor. *Materials* **2020**, *13*, 3234. [[CrossRef](#)]
34. Majumdar, D.; Singha, A.; Mondal, P.; Kundu, S. DNA-mediated wirelike clusters of silver nanoparticles: An ultrasensitive SERS substrate. *ACS Appl. Mater. Interfaces* **2013**, *5*, 7798–7807. [[CrossRef](#)]
35. Hong, S.; Li, X. Optimal size of gold nanoparticle for surface-enhanced Raman spectroscopy under different condition. *J. Nanomater.* **2013**, *2013*, 790323. [[CrossRef](#)]
36. Duval Malinsky, M.; Kelly, K.L.; Schatz, G.C.; Van Duyne, R.P. Nanosphere lithography: effect of substrate on the localized surface plasmon resonance spectrum of silver nanoparticles. *J. Phys. Chem. B* **2001**, *105*, 2343–2350. [[CrossRef](#)]
37. De Teresa, J.M. Introduction to nanolithography techniques and their applications. In *Nanofabrication. Nanolithography Techniques and Their Applications*, 1st ed.; De Teresa, J.M., Ed.; Ebook: Bristol, UK, 2020; pp. 1-1–1-28.
38. Dong, J.; Carpinone, P.L.; Pyrgiotakis, G.; Demokritou, P.; Moudgil, B.M. Synthesis of precision gold nanoparticles using turkevich method. *Kona* **2020**, *37*, 224–232. [[CrossRef](#)] [[PubMed](#)]
39. Bastús, N.G.; Merkoçi, F.; Piella, J.; Puntès, V. Synthesis of highly monodisperse citrate-stabilized silver nanoparticles of up to 200 nm: Kinetic control and catalytic properties. *Chem. Mater.* **2014**, *26*, 2836–2846. [[CrossRef](#)]
40. Bastús, N.G.; Comenge, J.; Puntès, V. Kinetically controlled seeded growth synthesis of citrate-stabilized gold nanoparticles of up to 200 nm: Size focusing versus Ostwald Ripening. *Langmuir* **2011**, *27*, 11098–11105. [[CrossRef](#)]
41. De Leon Portilla, P.; González, A.L.; Sanchez Mora, E. *Theoretical and Experimental Study on the Functionalization Effect on the SERS Enhancement Factor of SiO<sub>2</sub>-Ag Composite Films*; IntechOpen: London, UK, 2021; In Press. [[CrossRef](#)]
42. Chen, X.H.; Li, A.G.; Cai, J.H.; Yang, J.; Tuo, M. Absorption spectrum of carbon nanotubes in the space. *Sci. Sin.-Phys. Mech. Astron.* **2022**, *52*, 119512.
43. Romo-Herrera, J.M.; González, A.L.; Guerrini, L.; Castiello, F.R.; Alonso-Nuñez, G.; Contreras, O.E.; Alvarez-Puebla, R.A. A study of the depth and size of concave cube Au nanoparticles as highly sensitive SERS probes. *Nanoscale* **2016**, *8*, 7326–7333. [[CrossRef](#)]
44. Konokhova, A.I.; Gelash, A.A.; Yurkin, M.A.; Chernyshev, A.V.; Maltsev, V.P. High-Precision Characterization of Individual *E. coli* Cell Morphology by Scanning Flow Cytometry. *Cytometry A* **2013**, *83*, 568–575. [[CrossRef](#)]

45. Gienger, J.; Gross, H.; Ost, V.; Bär, M.; Neukammer, J. Assessment of deformation of human red blood cells in flow cytometry: Measurement and simulation of bimodal forward scatter distributions. *Biomed. Opt. Express* **2019**, *10*, 4531–4550. [[CrossRef](#)] [[PubMed](#)]
46. Draine, B.T. Graphite Revisited. *APJ* **2016**, *831*, 109. [[CrossRef](#)]
47. Purcell, E.M.; Pennypacker, C.R. Scattering and absorption of light by nonspherical dielectric grains. *Astrophys. J.* **1973**, *186*, 705–714. [[CrossRef](#)]
48. Goodman, J.J.; Draine, B.T.; Flatau, P.J. Application of fast-fourier-transform techniques to the discrete-dipole approximation. *Opt. Lett.* **1991**, *16*, 1198–1200. [[CrossRef](#)] [[PubMed](#)]
49. Kreibig, U. Electronic properties of small silver particles: The optical constants and their temperature dependence. *J. Phys. F Met. Phys.* **1974**, *4*, 999–1014. [[CrossRef](#)]
50. Ziegler, C.; Eychmüller, A. Seeded growth synthesis of uniform gold nanoparticles with diameters of 15–300 nm. *J. Phys. Chem. C* **2011**, *115*, 4502–4506. [[CrossRef](#)]
51. Njoki, P.N.; Lim, I.-S.; Mott, D.; Park, H.Y.; Khan, B.; Mishra, S.; Sujakumar, R.; Luo, J.; Zhong, C.J. Size correlation of optical and spectroscopic properties for gold nanoparticles. *J. Phys. Chem. C* **2007**, *111*, 14664–14669. [[CrossRef](#)]
52. Espina, A.; Cañamares, M.V.; Juraseková, Z.; Sanchez-Cortes, S. Analysis of Iron Complexes of Tannic Acid and Other Related Polyphenols as Revealed by Spectroscopic Techniques: Implications in the Identification and Characterization of Iron Gall Inks in Historical Manuscripts. *ACS Omega* **2022**, *7*, 27937–27949. [[CrossRef](#)]
53. Noguez, C.; Villagómez, C.J.; González, A.L. Plasmonics of multifaceted metallic nanoparticles, field enhancement, and TERS. *Phys. Status Solidi B* **2015**, *252*, 56–71. [[CrossRef](#)]
54. Borah, M.M.; Devi, T.G. Vibrational studies of thyroxine hormone: Comparative study with quantum chemical calculations. *J. Mol. Struct.* **2017**, *1148*, 293–313. [[CrossRef](#)]
55. Rizzon, R.V.K.; Ludwing, Z.M.C.; Modesto-Costa, L.; Ludwing, V. Thyroxine: A theoretical study of the vibrational and electronic properties. *QUARKS Braz. Electron. J. Phys. Chem. Mat. Sci.* **2020**, *3*, 31–40.
56. Álvarez, R.M.; Della Védova, C.O.; Mack, H.G.; Fariás, R.N.; Hilderbrandt, P. Raman spectroscopic study of the conformational changes of thyroxine induced by interactions with phospholipid. *Eur. Biophys. J.* **2002**, *31*, 448–453. [[CrossRef](#)] [[PubMed](#)]
57. Mandak, V.; Gupta, S.K.; Jha, P.K.; Ovsyuk, N.N.; Kachurin, G.A. Low-frequency Raman scattering from Si/Ge nanocrystals in different matrixes caused by acoustic phonon quantization. *J. Appl. Phys.* **2012**, *112*, 054318.
58. Lombardi, J.R.; Birke, R.L. A unified view of surface-enhanced Raman scattering. *Acc. Chem. Res.* **2009**, *42*, 734–742. [[CrossRef](#)]
59. Kho, K.W.; Dinish, U.S.; Kumar, A.; Olivo, M. Frequency shifts in SERS for biosensing. *ACS Nano* **2012**, *6*, 4892–4902. [[CrossRef](#)]
60. Wang, Y.; Yu, Z.; Ji, W.; Tanaka, Y.; Sui, H.; Zhao, B.; Ozaki, Y. Enantioselective discrimination of alcohols by hydrogen bonding: A SERS study. *Angew. Chem. Int. Ed.* **2014**, *53*, 13866–13870. [[CrossRef](#)]
61. Zhang, X.; Liu, Y.; Soltani, M.; Li, P.; Zhao, B.; Cui, B. Probing the interfacial charge-transfer process of uniform ALD semiconductor-molecule-metal models: A SERS study. *J. Phys. Chem. C* **2017**, *121*, 26939–26948. [[CrossRef](#)]
62. Ma, H.; Liu, S.; Zheng, N.; Liu, Y.; Han, X.X.; He, C.; Lu, H.; Zhao, B. Frequency shifts in surface-enhanced Raman spectroscopy-based immunoassays: Mechanistic insights and application in protein carbonylation detection. *Anal. Chem.* **2019**, *91*, 9376–9381. [[CrossRef](#)]
63. Thermo Fisher Scientific. Thyroxine (T<sub>4</sub>) Competitive ELISA Kit. Available online: [https://www.thermofisher.com/document-connect/document-connect.html?url=https://assets.thermofisher.com/TFS-Assets%2FMSG%2Fmanuals%2FEIAT4\\_C\\_Thyroxine\\_Competitive\\_Rev1\\_31Jan2017\\_web.pdf](https://www.thermofisher.com/document-connect/document-connect.html?url=https://assets.thermofisher.com/TFS-Assets%2FMSG%2Fmanuals%2FEIAT4_C_Thyroxine_Competitive_Rev1_31Jan2017_web.pdf) (accessed on 10 July 2023).
64. Li, D.D.; Timchenko, V.; Chan, Q.N.; Yuen, A.C.Y.; Yeoh, G.H. Study of morphology and optical properties of gold nanoparticle aggregates under different pH conditions. *Langmuir* **2018**, *34*, 10340–10352. [[CrossRef](#)]

**Disclaimer/Publisher’s Note:** The statements, opinions and data contained in all publications are solely those of the individual author(s) and contributor(s) and not of MDPI and/or the editor(s). MDPI and/or the editor(s) disclaim responsibility for any injury to people or property resulting from any ideas, methods, instructions or products referred to in the content.